ACS MEASUREMENT SCIENCE Au
AN OPEN ACCESS JOURNAL OF THE AMERICAN CHEMICAL SOCIETY

pubs.acs.org/measureau
Article

Simultaneous Imaging of Temperature and Oxygen by Utilizing Thermally Activated Delayed Fluorescence and Phosphorescence of a Single Indicator

Published as part of ACS Measurement Science Au special issue "2024 Rising Stars".

Georg Schwendt, Andrey V. Kalinichev, Sergey M. Borisov,* and Klaus Koren*

Cite This: ACS Meas. Sci. Au 2024, 4, 568−576
Read Online

ABSTRACT: Chemical gradients are essential in biological systems, affecting processes like microbial activity in soils and nutrient cycling. Traditional tools, such as microsensors, offer high-resolution data but are limited to one-dimensional measurements. Planar optodes allow for two-dimensional (2D) and three-dimensional (3D) chemical imaging but are often sensitive to temperature changes. This study presents an advanced dual-emission optical sensor that simultaneously measures temperature and oxygen using a modified platinum(II) meso-tetrakis(3,5-di*tert*-butylphenyl)-tetra(2-*tert*-butyl-1,4-naphthoquinono)porphyrin. The ratio between thermally activated delayed fluorescence and phosphorescence was optimized by modifying platinum(II) naphthoquinonoporphyrin with *tert*-butyl groups which simultaneously improved solubility in apolar solvents and polymer matrix (polystyrene). This dual-function sensor enables two-parameter chemical imaging with a consumer-grade RGB camera or a hyperspectral camera. We demonstrated 2D visualization of temperature and oxygen distribution in a model soil system. The RGB camera provided rapid and cost-effective imaging, while the hyperspectral camera offered more detailed spectral information despite some limitations. Our findings revealed the formation of a stable temperature gradient and oxygen depletion, driven by water content and temperature-sensitive microbial activity. This dual O_2/T sensor, with further potential improvements, shows considerable promise for advanced multiparameter sensing in complex biological and environmental studies, providing deeper insights into dynamic microenvironments.

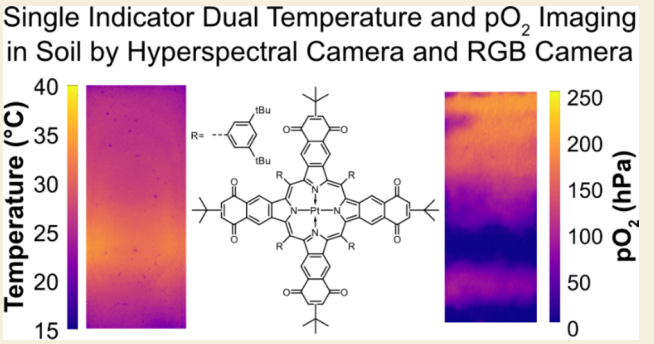

KEYWORDS: *multiparameter analysis, optical sensors, chemical imaging, partial least-squares regression, chemical gradients, hyperspectral imaging, TADF*

1. INTRODUCTION

Chemical gradients are ubiquitous in biological systems.[1,2] From biofilms to soils it is well understood that biological activity and transport processes shape the chemical microenvironment in time and space.[3−5] This microscale heterogeneity is in part utilized in biotechnology (e.g., wastewater treatment)[6] and has important implications for global nutrient cycles or adaptations of certain organisms.[7]

Nevertheless, measuring or even better visualizing heterogeneities in biological systems is still challenging. While microsensors have the potential to measure at high spatial and temporal resolution, they are limited to one-dimensional (1D) measurements.[8,9] Chemical imaging, on the contrary, can provide two-dimensional (2D) or three-dimensional (3D) chemical images by utilizing luminescent molecules as receptors within chemical sensors, so-called optodes.[10,11] In recent years it has been demonstrated that optodes can be useful tools to study chemical dynamics in complex biological systems ranging from sediments[12] to plants[13] and even animals.[14,15] Even further, beyond biological systems, optode technology is used in the form of pressure-sensitive paints to visualize pressure gradients on man-made structures.[16]

A key limiting factor of all those measurements is the intrinsic cross-sensitivity of every optical sensor to temperature.[17] Consequently, temperature needs to be either stable during the analysis or compensated for. Maintaining stable temperature is difficult in many biological systems as metabolic activity itself creates heat.[18] Furthermore, natural systems often

Received: July 12, 2024
Revised: August 29, 2024
Accepted: August 29, 2024
Published: September 5, 2024

https://doi.org/10.1021/acsmeasuresciau.4c00040
ACS Meas. Sci. Au 2024, 4, 568−576

exhibit large- or small-scale temperature gradients like within the water column or within the soil profile.[19] These factors underscore the importance of temperature compensation in chemical imaging in biological systems.

Over the years temperature optodes have been developed that enable the 2D visualization of temperature.[17,20,21] Most often those sensors are based on phosphorescent indicators encapsulated in an O_2 impermeable material (polymer). As temperature affects all luminescent materials, though to a varying degree, shielding an indicator from other quenchers enables temperature imaging with optode technology. Those sensors are only sensitive to temperature and as such need to be combined with other chemical sensors to enable chemical imaging.[22] So far only a limited number of examples exist where temperature and another chemical parameter have been imaged using a single sensor.[20,23−25]

More recently a new class of sensor material has emerged which combines temperature sensing with oxygen sensing using a single indicator, although such materials are still rare.[25−28] Among them, metallobenzoporphyrins stand out due to their high molar absorption coefficients of their B- and Q-bands (usually located in the blue to green and orange to red parts of the electromagnetic spectrum, respectively), and their high emission wavelengths (red to NIR). The decay time of long-lived phosphorescence (emission from excited triplet state) or thermally activated delayed fluorescence (TADF, emission from excited singlet state after occurrence of reverse intersystem crossing from excited triplet state) can be used to determine the oxygen concentration, while the ratio of either TADF to prompt fluorescence[25] (emission from excited singlet state without intersystem crossing) or the ratio of TADF to phosphorescence[26,29] can be used to determine temperature. While prompt fluorescence and TADF show the same spectral characteristics, TADF and phosphorescence occur at different wavelengths (phosphorescence at lower energy than TADF). Although these two types of emission are exceptionally well separated in Pd(II) and Pt(II) benzoporphyrins, their emissions are not compatible with standard color cameras, featuring red, green, and blue coatings on the CCD or CMOS chips, which have recently emerged as cheap and easy to use options in chemical imaging.[30] Monochrome cameras with appropriate filters are a possible solution. Changing filters requires manual labor, which is error-prone and costly, or the use of a mechanical filter wheel which introduces an additional mechanical part. Alternatively, hyperspectral cameras can be used. Hyperspectral cameras use spectral filtering units in front of the CCD or CMOS chip and as such enable the recording of full spectra in every pixel of the image. We have shown that this type of imaging system can be used in chemical imaging and that it allows for spectral unmixing and machine learning-based analysis.[31,32] So far, hyperspectral imaging has not been used to study materials that simultaneously emit TADF and phosphorescence.

In this study, we developed an improved TADF and phosphorescence-based indicator for the combined imaging of temperature and O_2. Hyperspectral chemical imaging as well as filter based spectral selection was tested to generate chemical images. As a test case an artificial temperature gradient within a soil sample was generated. As microbial activity is temperature-dependent, we expected to see increased respiration in areas with higher temperatures.

2. EXPERIMENTAL SECTION

2.1. Materials

Unless otherwise noted, all substances were used as received.

Toluene (HPLC+ grade) and hexamethyldisiloxane were bought from Sigma-Aldrich, 2-*tert*-butyl-1,4-benzoquinone was acquired from TCI-Europe, *n*-heptane (analytical grade) and sodium dithionate were obtained from Merck, triethylamine (≥99.5% purity) and chloroform (purity >99%, stabilized with 0.4−1% ethanol) were bought from Carl Roth. The reference dye Lumogen F Orange (*N*,*N*-bis(2,6-diisopropylphenyl)perylene-3,4,9,10-bis(dicarboximide)) was bought from Kremer Pigmente. Polystyrene (PS, average M.W. 260 kDa) was obtained from Acros Organics, and monocrystalline diamond powder (1−2 μm) was obtained from Microdiamant. Silicone E43 was obtained from Wacker Chemie. Chloroform-D3 was acquired from Eurisotop. The sandy loam-type soil collected in Åstrup (Denmark) was sieved (2 mm) prior to use (further details on the soil can be found in the Supporting Information).

2.2. Methods

Optical measurements were performed in dark rooms.

Luminescence spectra were recorded on a Fluorolog 3 spectrofluorometer (Horiba Scientific) equipped with an R2658 photomultiplier (Hamamatsu). Luminescence decay times were measured on the same spectrometer equipped with a DeltaHub module (Horiba) using a SpectraLED excitation source (λ = 456 nm, Horiba). Data analysis was performed on DAS-6 analysis software (Horiba) applying a mono- or a biexponential fit function. Average decay times (τ) of biexponential fits were calculated from the relative amplitudes (B_1, B_2) and lifetimes (τ_1, τ_2) using the equation $\tau = B_1 \times \tau_1 + B_2 \times \tau_2$.

NMR spectra were recorded on a 300 or 400 MHz NMR spectrometer from Bruker or JEOL, respectively. Chemical shifts are reported relative to the residual signals of the used deuterated solvent. High-resolution mass spectra were recorded on the matrix-assisted laser desorption/ionization time-of-flight mass spectrometer (MALDI-TOF MS) Micromass MALDI micro MX from Waters.

2.2.1. RGB Camera Settings. The imaging of optodes was conducted with a DSLR camera (EOS 2000D, Canon, Japan) with a removed NIR filter in combination with a macro-objective lens (AT-X M100 PRO D Macro, 100 mm f2.8, Tokina, Japan) with appropriate symmetric illumination in an otherwise dark room. The locations of the camera and the light sources were fixed throughout the experiments. The inverse relative aperture (*f*-number) was always *f*/2.8, ISO was 100. The exact imaging parameters and filters are shown in Table 1.

Table 1. Optical Filters and Shutter Times Used with the RGB Camera

signal	set of optical filters	shutter time (s)
reference	Calflex X (Qioptiq) 767 Oklahoma yellow (LEE Filters) 735 Velvet green (LEE Filters)	5
TADF	Calflex X (Qioptiq) 182 Light Red (LEE-Filters) R64 (Hoya)	4
phosphorescence	W-IR760 (Hoya)	2

2.2.2. Hyperspectral Camera Settings. The hyperspectral camera (imec SNAPSCAN VNIR) was mounted with a lens (Schneider Kreuznach, Apo-Xenoplan 2.0/24−0005) and equipped with an optical filter (767 Oklahoma yellow, LEE Filters) to exclude excitation light. The camera was stationary during the whole measurement and controlled by the manufacturer's software (HSI Snapscan v1.8.1.1). White balancing was performed according to the user manual with a 95% reflectance white reference (SphereOptics, Zenith Lite Diffuse Reflectance Target SG3151). Full-resolution corrected cubes (1088 × 2048) were acquired in discontinuous (stop

https://doi.org/10.1021/acsmeasuresciau.4c00040
ACS Meas. Sci. Au 2024, 4, 568−576

motion) mode with a step size of 3 pixels and an integration time of 800 ms. Pixel blur and binning were disabled.

For calibration, the sensor foil was taped to an inner wall of a homemade aquarium. The gaps between the glass wall and the sensor foil were filled with a thin water film. The aquarium was filled with water and equipped with a magnetic stir bar for mixing and a hollow metal coil used for cooling/heating by passing temperature-controlled water through it using a cryostat (Lauda Alpha RA 8). A Firesting GO2 (PyroScience) oxygen meter was used for readout of the reference temperature- (PyroScience TDIP15) and oxygen probes (PyroScience OXROB3). The calibration process started with air-saturated oxygen concentration, which was decreased stepwise by the addition of 5 wt % sodium dithionate solution at constant temperature. As an excitation source, a high-power 460 nm LED (LEDHub by Omicron-Laserage) was employed. Acquisition of images/cubes with the RGB- and hyperspectral camera was performed in parallel, using the settings described earlier.

2.3. Synthesis

Discussion about synthesis can be found in the Supporting Information.

2.3.1. *meso*-Tetrakis(3,5-di-*tert*-butylphenyl)-tetra(2-*tert*-butyl-1,4-naphthoquinono)porphyrin (H_2-*t*BuNQ). A reaction vial equipped with a magnetic stir bar was charged with 25.1 mg (17.6 μmol, 1 equiv) of sulfoleno porphyrin,[33] 69.2 mg (421 μmol, 24 equiv) of 2-*tert*-butyl-1,4-benzoquinone, 4 mL of toluene, and 100 μL of triethylamine. The reaction was conducted for 10 min at 200 °C in a "Monowave 50" synthesis reactor (Anton Paar). After cooling to room temperature, the main part of the reaction mixture was separated from the brown, sticky residue that stuck on the inner walls of the reaction vial. The solvent was removed under reduced pressure, and the residue was dissolved in a mixture of 10 mL *n*-heptane and 10 mL MeOH. The phases were separated, and the *n*-heptane phase was washed thrice with prewashed (with *n*-heptane) MeOH (3 × 10 mL). The solvent was removed under reduced pressure, and the residue was dried overnight at 65 °C under high vacuum, to yield 31 mg (97%) of H_2-*t*BuNQ, which was used in the next step without further purification. ^{1}H NMR (300 MHz, $CDCl_3$): δ 8.32−8.26 (m, 4H), 8.19−8.12 (m, 8H), 8.13−7.77 (m, 8H), 6.89−6.81 (m, 4H), 1.57−1.50 (m, 72H), 1.40−1.33 (m, 36H), (−0.53)-(−0.64) (m, 2H).

2.3.2. Platinum(II) *meso*-Tetrakis(3,5-di-*tert*-butylphenyl)-tetra(2-*tert*-butyl-1,4-naphthoquinono)porphyrin (Pt-*t*BuNQ). A reaction vial equipped with a magnetic stir bar was charged with 30.0 mg (16.5 μmol, 1 equiv) H_2-*t*BuNQ, 11.9 mg (25.2 μmol, 1.5 equiv) of dichlorobis(benzonitrile)platinum(II),[26] and 3 mL of toluene. The reaction was conducted for 15 min at 200 °C in a "Monowave 50" synthesis reactor (Anton Paar). After cooling to room temperature, the solvent was removed under reduced pressure. The residue was partially dissolved in *n*-heptane and filtered over Celite. The filtrate was applied to a *n*-heptane-conditioned silica gel column. Approximately 10 column volumes of *n*-heptane were passed through the column before the product was eluted with a minimal amount of $CHCl_3$. The product fractions were concentrated, and the residue was dried at 65 °C under high vacuum over the weekend to yield 30.9 mg (93%) of Pt-*t*BuNQ as a metallic dark green solid. ^{1}H NMR (300 MHz, $CDCl_3$) δ 8.32−8.29 (m, 4H), 8.08−8.04 (m, 8H), 7.94−7.90 (m, 4H), 7.87−7.83 (m, 4H), 6.87−6.84 (m, 4H), 1.56−1.52 (m, 72H), 1.40−1.36 (m, 36H). ^{13}C NMR (101 MHz, $CDCl_3$)*: δ 185.72, 184.08, 159.09, 153.08, 140.71, 140.00, 138.60, 137.07, 134.61, 130.50, 128.70, 127.19, 125.40, 125.11, 123.80, 122.18, 35.98, 35.56, 31.82, 29.54. *Highly complex spectrum due to isomers. For clarity, peak clusters are summarized as single peaks. MALDI-TOF: m/z [M^+] calc. for $C_{124}H_{132}N_4O_8Pt$, 2000.9723; found, 2000.9714.

2.4. Preparation of Sensing Materials

A sensor "cocktail" consisting of 1.410 g 10 wt % PS in $CHCl_3$, 117.5 μL of 3.0 g/L Pt-*t*BuNQ solution in $CHCl_3$, and 28.2 μL of a 2.5 g/L Lumogen F Orange solution in $CHCl_3$ was knife-coated onto a 125 μm thick transparent Melinex 506 poly(ethylene terephthalate) foil (Pütz Folien, Germany) using a 30 μm spacer, resulting in a maximum Q-band absorption of the dried foil less than 0.1 to avoid the inner-filter effect. After drying at room temperature for 2 h, another layer consisting of 2.08 g of diamond powder, 4.04 g hexamethyldisiloxane, and 3.12 g of silicone E43 was knife-coated on top of the sensor layer with a 90 μm spacer. After air drying for 1 h, the foil was further dried at 70 °C overnight.

3. RESULTS AND DISCUSSION

Otto S. Wolfbeis underlined that "sensors are much(!) more than just a molecule, and most are of the stand-alone type".[34] While a receptor, in this case, the indicator dye, is the heart of a sensor this indicator needs to be embedded in an appropriate matrix and be detected using the proper optical setup. Due to this essential consideration, this study will describe the sensor development from the indicator to the material and finally to the imaging system.

3.1. Choice of Materials

We considered the recently published dually emitting palladium and platinum benzoporphyrins[29] as indicator dyes for this work. These dyes can be excited in the blue-green and red parts of electromagnetic spectrum and emit red to near-infrared light through both TADF and phosphorescence mechanisms with both emissions being spectrally well separated from each other. Since the spectral characteristics of the available indicator dyes are very similar, the selection of the indicator dye was based primarily on the TADF to phosphorescence ratio, quantum yield, (photo)chemical stability, and compatibility with common polymer matrices. The platinum(II) benzoporphyrins show roughly double the quantum yield of their palladium counterparts, and, as oxygen indicators, they usually feature an advantageous dynamic range in polystyrene for measurements from hypoxic conditions to ambient oxygen levels. The candidate with the highest TADF to phosphorescence ratio (0.21 at 25 °C), the platinum(II) naphthoquinonoporphyrin, has unprotected double bonds, leading to decreased photostability, and questionable chemical stability. The platinum(II) anthraquinonoporphyrin overcomes this limitation but only shows around half the TADF to phosphorescence ratio (0.10). To utilize the higher TADF to phosphorescence ratio while mitigating the stability issues of the naphthoquinonoporphyrin, we sterically protected the double bonds by introducing *tert*-butyl groups. The resulting Pt-*t*BuNQ complex (Figure 1) showed an intermediate TADF

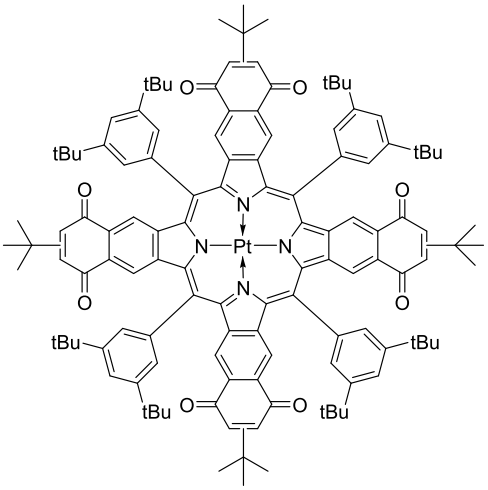

Figure 1. Chemical structure of the new porphyrin indicator Pt-*t*BuNQ.

https://doi.org/10.1021/acsmeasuresciau.4c00040
ACS Meas. Sci. Au 2024, 4, 568−576

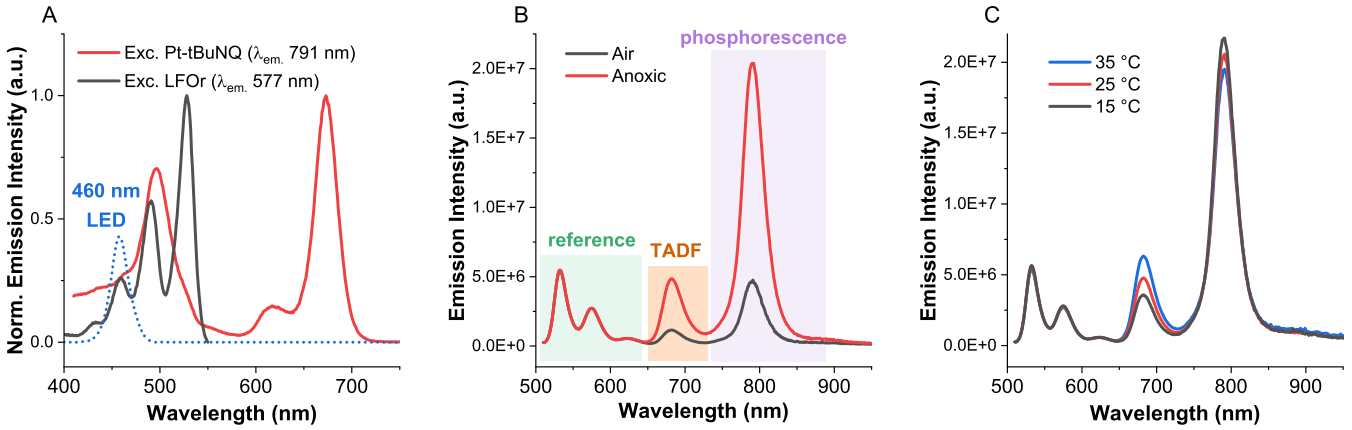

Figure 2. Spectral characteristics of the dually sensing optode. A: Excitation spectrum of Pt-*t*BuNQ (red) and LFOr (black) in PS; emission spectrum of the used LED with λ_{max} = 460 nm (blue). B: Luminescence in air-saturated water and in 10 wt % Na_2SO_3 solution (anoxic) at 25 °C (excitation wavelength 490 nm). C: Temperature dependency of the emission spectra under anoxic conditions.

to phosphorescence ratio (0.17 at 25 °C), and drastically improved solubility in apolar solvents. Furthermore, the synthesis of quinone-extended porphyrins and their platination could be significantly improved, resulting in decreased synthetic effort and higher yields (details can be found in the Supporting Information).

In order to enable oxygen measurements alongside temperature measurements using cameras without lifetime-imaging capabilities, addition of an oxygen- and temperature-insensitive reference dye is necessary. We chose the fluorescent perylene bisimide derivative "Lumogen F Orange" (LFOr) due to its excellent spectral compatibility with the indicator (as shown in Figure 2), chemical and photochemical stability, and brightness.

3.2. Optical Characterization

The optical characteristics of the optode material are summarized in Figure 2. The excitation spectra of the indicator and reference dye show broad overlap in the blue-green wavelength region, with the optimal excitation wavelength around 490 nm (Figure 2A, actual excitation wavelength 460 nm). While the indicator shows a strong response to both oxygen and temperature (Figure 2B,C, respectively), the reference dye shows negligible dependence on either parameter. Additionally, decay time measurements of the indicator in PS with and without reference dye were performed (Figure S1). Under anoxic conditions at 25 °C, both measurements resulted in a decay time of 39 μs, indicating that no energy transfer from the indicator to the reference dye takes place under these conditions.

3.3. Imaging Approaches

Our optode shows an excellent spectral separation of all signals (reference, TADF, and phosphorescence, Figure 2B). This allows us to use not only a hyperspectral (HS) camera with high spectral resolution but also a conventional RGB or monochrome camera combined with different spectral filters. As shown previously,[29] we expected the TADF to phosphorescence ratio to follow an Arrhenius-like dependence on temperature,[35] while both TADF and phosphorescence are expected to be quenched equally by molecular oxygen. Due to incorporation of the indicator into a polymer matrix, we expected the dynamic quenching behavior to follow a modified Stern–Volmer equation, the so-called two-site model.[36]

3.3.1. Calibration - Hyperspectral Camera.

As spatial region of interest, we chose a 20 × 20-pixel area located at the reference temperature and oxygen sensors. The spectral region of interest was selected by visual inspection of the obtained averaged spectra and the standard deviations of the spectral bands (Figure 3). Additional considerations were made for our

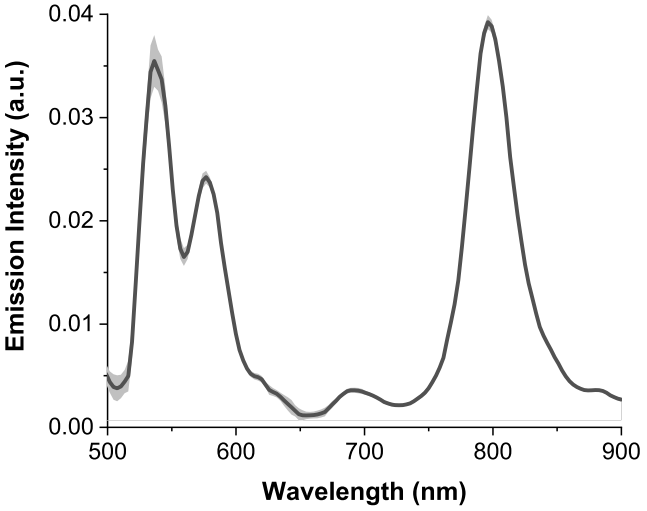

Figure 3. Example calibration spectrum (mean values and corresponding standard deviations at 24.4 °C and 123 hPa pO_2) from the 20 × 20-pixel spatial ROI where the reference sensors were placed.

specific HS camera, which has a stepped filter layout with two distinct spectral filter regions (470–625 and 625–900 nm), and requires a complicated correction algorithm.[37] It was previously found in literature[38] that for reliable referencing with this camera it is necessary to have a reference dye that emits in the same spectral filter region as the indicator. Some part of the reference emission falls into the same filter zone as the indicator emissions. This is however very close to the overlap region of the spectral filter zones (~600–650 nm) which shows poor signal quality as previously noted in literature.[31] Therefore, we chose the spectral region spanning the bands closest to 562–608 nm for the reference signal, despite being in a different spectral filter zone than the indicator emission. For TADF, we chose the spectral region

https://doi.org/10.1021/acsmeasuresciau.4c00040
ACS Meas. Sci. Au 2024, 4, 568–576

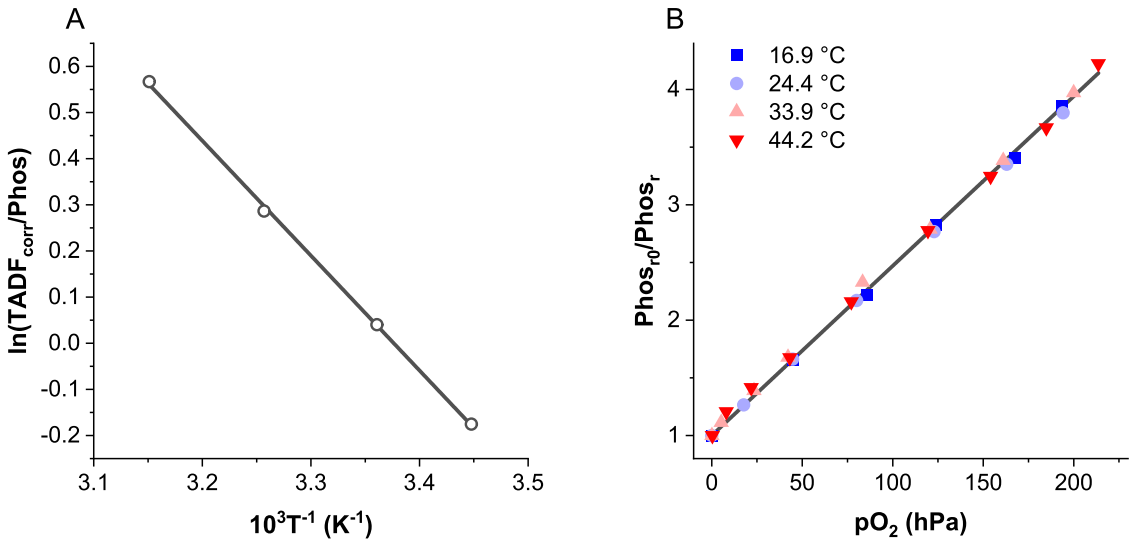

Figure 4. Calibration functions for temperature (A) and oxygen partial pressure (B).

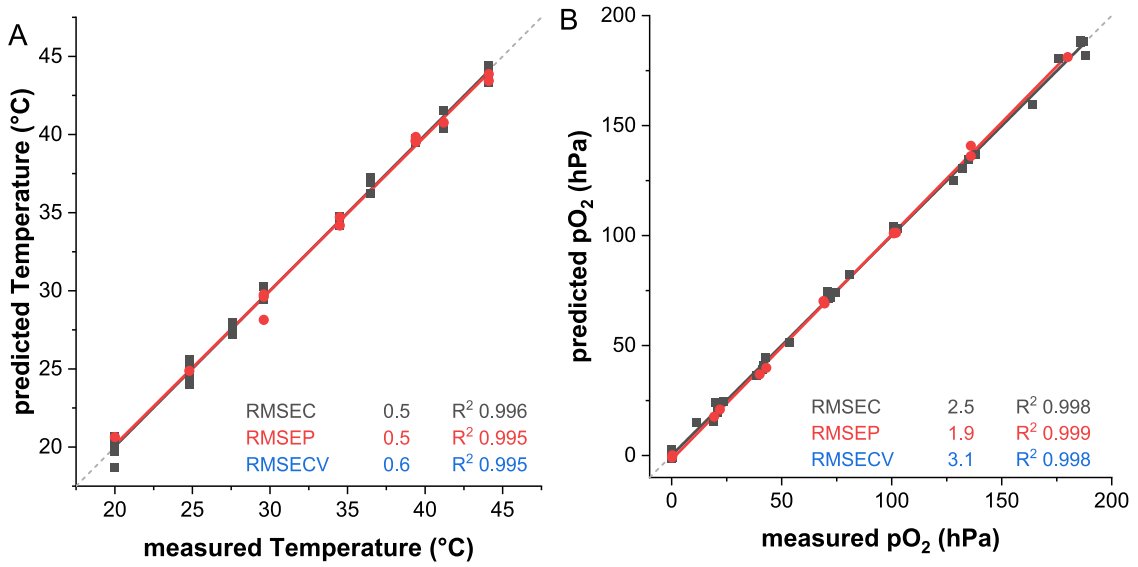

Figure 5. Scatter plots of actual vs predicted values for temperature (A) and oxygen (B) determination. R^2 and Root Mean Squared Errors (RMSE) are shown in the plots.

spanning the bands closest to 672−727 nm. In the first calibration, we found that the signal of the TADF emission was too low at higher oxygen concentrations to be measured reliably. Therefore, the calibration was repeated. To increase the TADF signal, the phosphorescence emission was partially oversaturated at wavelengths below 860 nm, which explains why we chose to use the spectral region spanning the bands closest to 860−900 nm for the phosphorescence signal. The selected spectral regions were integrated using the trapezoidal rule.

The TADF signal was found to contain background fluorescence (from the reference dye and aquarium glass) and was corrected by subtracting a constant fraction (2%) of the reference signal, yielding $TADF_{corr}$.

The results of the second calibration are shown in Figure 4. The temperature data was fitted according to an Arrhenius plot (Figure 4A, $R^2 > 0.999$), and is independent of the reference signal, except for a small correction factor in the TADF signal. In contrast, the indicator luminescence for oxygen measurements needs to be referenced. While ideally the whole indicator luminescence should be used for oxygen measurements, we opted to only use the phosphorescence signal (divided by the reference signal, denoted $Phos_r$), due to better signal quality. Surprisingly, the oxygen calibration data could be excellently fitted (Figure 4B, $R^2 > 0.999$) using the ideal Stern−Volmer plot rather than the two-site model.[36] Even more surprisingly, the oxygen calibration showed no apparent temperature dependence with a K_{SV} value of 0.0147 hPa^{-1} for all calibration temperatures. We assume that the low signal intensity in combination with potential artifacts arising from the complicated correction algorithm[37] needed for our type of HS camera, are responsible for the observed behavior.

3.3.2. Calibration - RGB Camera. In addition, we decided to use a conventional RGB camera (with the removed NIR filter) combined with spectral filters due to the excellent spectral separation between TADF and phosphorescence emissions. In the proposed approach, the RGB camera captures 3 individual photographs corresponding to different

https://doi.org/10.1021/acsmeasuresciau.4c00040
ACS Meas. Sci. Au 2024, 4, 568−576

spectral regions as shown in Figure 2: the fluorescence from the reference indicator (R), the TADF signal (F), and the phosphorescence from the indicator dye (P). The captured images have 3-color channels ($_R$—red, $_G$—green, and $_B$—blue), represented as 8-bit raw intensity values, resulting in 9 variables initially. Subsequently, we excluded R_R, R_B, F_G, and F_B signals due to their low intensity and high probability of capturing noise. In contrast, the signal intensities of P_R, P_B, and P_G were all sufficient due to the removal of the NIR filter and the overlapping spectral sensitivity of distinct R, G, and B channels.[39] To address the issue of nonlinear responses, we expanded the variable space by calculating all possible ratios between individual channels and their log values, resulting in 45 variables. Therefore, we had a complex data set with nonlinear responses that were not easily interpretable using simple linear models. Moreover, the signals obtained from different filters could be highly collinear, meaning they are correlated and do not vary independently. Due to these factors, we opted for partial least squares regression (PLSR).

To simultaneously determine O_2 and T, two separate models with different variables were built: one for O_2 measurement and another for T measurement. In contrast to a combined model for both variables (PLS2) each model can independently optimize the prediction of its specific response variable. The steps involved training the PLSR model using calibration data (36 points) that included known values of temperature and oxygen concentration along with the corresponding image intensities. The trained PLSR model was then validated with a separate data set (15 points, approximately 30% of the initial data set) to ensure its accuracy and reliability. The variables were chosen using the recursive weighted PLS method (rPLS).[40] The robustness of the developed models was checked via cross-validation (CV) using the random subsets method with 10 data splits and 5 iterations. Once validated, the model was applied to the experimental images to extract quantitative information about temperature and oxygen gradients.

Figure 5 shows scatter plots of measured vs predicted values for the calibration (C) and external test data sets (P).

Using rPLS resulted in 9 variables (R_G, F_R/P_R, F_R/P_B, F_R/R_G, P_R/F_R, P_G/F_R, P_G/R_G, R_G/P_R, R_G/P_G) for temperature calibration and 8 variables (R_G, F_R/P_R, P_R/F_R, P_R/R_G, P_B/P_G, R_G/T_R, R_G/P_G, R_G/P_B) for O_2 calibration.

For temperature, the root-mean-square error of calibration (RMSEC) is 0.5 °C, with an R^2 value of 0.996, demonstrating an excellent fit to the calibration data. The root-mean-square error of prediction (RMSEP) is 0.5 °C, and the root-mean-square error of cross-validation (RMSECV) is 0.6 °C, both maintaining an R^2 of 0.995. This consistency highlights the model's robustness and reliability when validated with independent data sets.

Similarly, the RMSEC is 2.5 hPa with an R^2 of 0.998 for oxygen. The RMSEP is 1.9 hPa, and the RMSECV is 3.1 hPa, with R^2 values of 0.999 and 0.998, respectively. These metrics confirm the model's high accuracy and robustness.

3.4. Application

3.4.1. Measurement Setup. The optode was taped to an inner glass wall of an aquarium. The aquarium was tightly packed with soil and contained a horizontally placed metal pipe connected to tubing, which was insulated by foam, to enable heating the soil around the pipe by 40 °C-hot water flow, as shown in Figure 6 (dimensions are depicted in Figure S2). In this way, a vertical temperature gradient was introduced into the measured system. The oxygen gradient formed naturally upon water addition to the soil. The sensor foil was illuminated by constant light intensity from a 460 nm high-power LED during the parallel acquisition of RGB images and hyperspectral cubes.

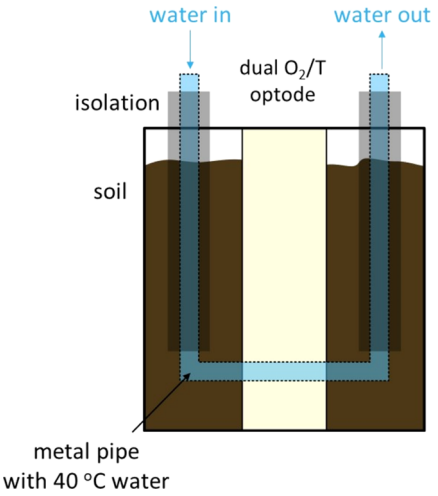

Figure 6. Scheme of used setup. A vertical temperature gradient is introduced by pumping hot water through the metal pipe.

3.4.2. Results. From the RGB- and HS-camera measurements, simultaneous O_2 and T 2D visualization was performed. Figure 7 illustrates the temperature gradient formation in a soil sandwich with a water pipe system, through which hot water at 40 °C was circulated within 19 h; to reduce water evaporation the soil chamber was covered with parafilm. While the obtained images from both cameras look very similar and reveal the same patterns, quantitative description is based on the more thoroughly characterized RGB camera measurements.

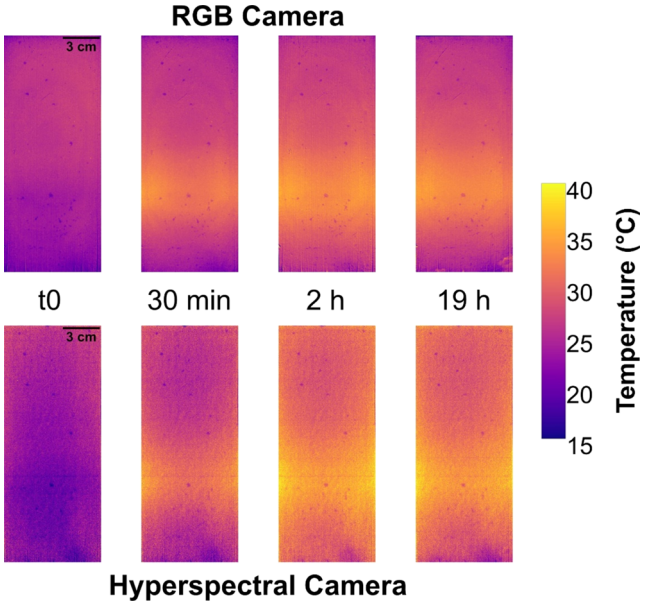

Figure 7. Time-lapse thermal imaging of heat transfer in soil with an embedded water pipe. Captions denote the time after the initiation of hot water flow.

https://doi.org/10.1021/acsmeasuresciau.4c00040
ACS Meas. Sci. Au 2024, 4, 568−576

Prior to the initiation of hot water flow, the temperature distribution is uniform and corresponds to room temperature (around 25 °C). As time progresses, there is a noticeable increase in temperature around the metal pipe area, demonstrating the heat transfer from the hot water to the surrounding soil. The temperature within the soil sandwich reached a steady state shortly after 30 min. The area closest to the pipe reached 34 ± 1 °C, which is close to that of the water itself, while the upper and lower edge of the soil sandwich remained close to room temperature. As expected, a steady temperature gradient from the metal pipe to the upper and lower edges is observed.

Figure 8 depicts the changes in oxygen partial pressure at various stages of the experiment. After the initial heating

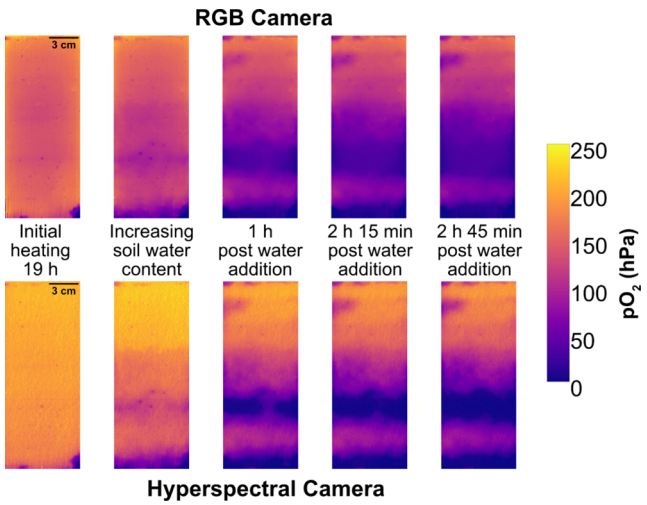

Figure 8. Sequential 2D visualization of oxygen partial pressure in a soil sandwich with a heated water pipe, indicating the impact of temperature, time, and soil water content on soil oxygen levels.

period of 19 h, most of the soil sandwich showed a uniform oxygen distribution (139 ± 13 hPa) corresponding to a rather well-aerated soil profile under atmospheric pressure, despite a relatively high initial soil water content of 25%. The first signs of deoxygenation start at the very bottom of the aquarium.

Air-saturated water was added continuously from the top in four portions (three of 50 mL each, and 20 mL for the last addition). The water passed through the soil slowly and no effect on temperature was observed. The total addition of 170 mL of water increased the soil water content to 32%, leading to a gradual decrease in the oxygen level. This effect was more significant in the vicinity of the water pipe, where the temperature was higher than in the surrounding areas.

This observed pattern of oxygen depletion can be attributed to several factors. First, the infusion of water fills the air-filled soil pores. Second, the water partial pressure increases with temperature, leading to a decreased pO_2 in warmer areas. Third, the elevated temperature around the pipe may accelerate microbial activity and oxygen consumption, leading to localized areas of lower oxygen levels and hotspots within the soil.[4]

In fact, temperature has a well-known impact on microbial respiration and growth. Although some microbes are adapted to growing at low temperatures, most soil microbes thrive at elevated temperatures.[41] As surface temperatures increase, the microbial growth rate can impact soil terrestrial biogeochemical processes and feedback mechanisms within the soil.[42] This laboratory experiment simulates such an increase in soil temperature and therefore it can help study bacterial responses to changing climate via direct measurement of both soil temperature and O_2 levels, which in turn are linked to respiration.

3.5. Comparison of Measurement Methods

Both measurement methods reveal the same trends in the soil experiment (see Figures 7 and 8), despite being vastly different. Both measurement methods have distinct advantages and disadvantages. The RGB camera with a removed NIR filter is inexpensive. It offers quicker image acquisition compared to the HS camera, but it only features three color channels compared to ≥150 bands in the used HS camera. The color channels of the RGB camera do not match the spectrum of our sensor foil, which means that additional optical filters need to be placed in front of the RGB camera. However, that also gives the possibility to individually set the integration time for each signal, and, for each manually placed filter, we get information from three color channels which proved useful in the building of the PLSR model. It should be noted that this could also be achieved using a monochrome camera, but without obtaining the additional spectral information from the other channels.

The HS camera is much more expensive and offers slower acquisition times, and, in our specific setup, the low TADF to phosphorescence ratio of the indicator (among other already discussed factors) makes reliable quantitative measurements a challenging task. Future improvements of the indicators TADF to phosphorescence ratio (or using the Pd(II) indicator analog in a less oxygen-permeable matrix) and/or instrumentation could overcome this limitation and enable measurements at temperatures below 15 °C. In general, spectral data in hyperspectral imaging allows for a high amount of flexibility in dealing with complex tasks. For example, overlapping signals can be unmixed/deconvoluted,[31] additional intrinsic optical information on biological samples can be gained,[38] and machine learning[32] can be employed in multidye optodes with complex spectral cross-interferences which would be inaccessible with conventional methods. This allows indicators for more parameters, with partially overlapping spectra and spectral cross-interferences, to be combined into multiparameter sensing materials. We expect such multiparameter sensing materials to become increasingly relevant in conjunction with hyperspectral imaging to unravel complex, intertwined processes in various research fields, while RGB cameras present an affordable alternative for less demanding tasks and will allow for a broader distribution of the methodology.

4. CONCLUSIONS

A new dually emitting indicator for simultaneous temperature and oxygen measurements was synthesized and incorporated into an optode. The indicator can be efficiently excited in the blue-green- and red regions of the visible spectrum and shows bright dual emission of TADF and phosphorescence that can be used for temperature determination. The oxygen concentration can be assessed by dynamic quenching of the long-lived excited triplet state. The previously reported synthesis procedure[29] (for similar compounds) was simplified and improved in yield. In comparison to the previously reported best-performing indicator (platinum(II) anthraquinonoporphyrin),[29] the TADF to phosphorescence ratio was increased

https://doi.org/10.1021/acsmeasuresciau.4c00040
ACS Meas. Sci. Au 2024, 4, 568−576

by a factor of 1.7. The introduced *tert*-butyl groups significantly improved solubility in apolar solvents and provide steric shielding from chemical attack on the quinone double bonds.

As a proof of concept, soil measurements with artificial temperature gradients and naturally forming oxygen gradients were performed using an RGB camera with a removed NIR filter, and an HS camera. A clear positive correlation between oxygen depletion rate (corresponding to microbial growth) and temperature was observed within the soil sample. The still moderate indicator TADF to phosphorescence ratio of 0.17 (at 25 °C) proved to be the main bottleneck in the HS measurements. With improvements in indicator and/or instrumentation, and with the help of the rapidly growing field of artificial intelligence, we expect similar indicators to be incorporated into multiparameter sensing materials for researching complex, intertwined processes in complex biological matrices.

Going back to Wolfbeis and his statement on a sensor being more than just the molecule, we believe this study nicely shows how the indicator (receptor) and the measurement setup play together. Improvements in either of them can result in new possibilities. Improving the indicator for sure will improve the sensor system as a whole. At the same time, HS imaging has only been possible for a rather short time and only recently it has been discovered for chemical sensing. This new imaging mode with all the data it provides is ideally suited to feed advanced chemometrics and artificial intelligence models. However, even with advanced data treatment, the interplay between sensing material and measurement setup will ultimately limit the quality of results.

■ ASSOCIATED CONTENT

Supporting Information

The Supporting Information is available free of charge at https://pubs.acs.org/doi/10.1021/acsmeasuresciau.4c00040.

Experimental details synthesis; soil characterization; sketch of setup with measures; ^{1}H NMR and MS spectra for all compounds (PDF)

■ AUTHOR INFORMATION

Corresponding Authors

Sergey M. Borisov − *Institute of Analytical Chemistry and Food Chemistry, Graz University of Technology, 8010 Graz, Austria;* orcid.org/0000-0001-9318-8273; Email: sergey.borisov@tugraz.at

Klaus Koren − *Department of Biology—Microbiology, Aarhus University Centre for Water Technology, 8000 Aarhus C, Denmark;* orcid.org/0000-0002-7537-3114; Email: klaus.koren@bio.au.dk

Authors

Georg Schwendt − *Institute of Analytical Chemistry and Food Chemistry, Graz University of Technology, 8010 Graz, Austria*

Andrey V. Kalinichev − *Department of Biology—Microbiology, Aarhus University Centre for Water Technology, 8000 Aarhus C, Denmark;* orcid.org/0000-0002-3233-8183

Complete contact information is available at: https://pubs.acs.org/10.1021/acsmeasuresciau.4c00040

Notes

The authors declare no competing financial interest.

■ ACKNOWLEDGMENTS

We thank Theresa Merl for providing characterized soil for the measurements and Lars B. Pedersen for technical assistance. The authors acknowledge support from the Grundfos Foundation (KK) and via a research grant (VIL50075) (KK) from Villum Fonden. This research was funded in part by the Austrian Science Fund (FWF) 10.55776/P32079−N37. For the purpose of open access, the authors have applied a CC BY public copyright license to any Author Accepted Manuscript version arising from this submission.

■ REFERENCES

(1) Kühl, M.; Cohen, Y.; Dalsgaard, T.; Jørgensen, B.; Revsbech, N. Microenvironment and Photosynthesis of Zooxanthellae in Scleractinian Corals Studied with Microsensors for O2, pH and Light. *Mar. Ecol. Prog. Ser.* **1995**, *117*, 159−172.

(2) Stewart, P. S.; Franklin, M. J. Physiological Heterogeneity in Biofilms. *Nat. Rev. Microbiol.* **2008**, *6* (3), 199−210.

(3) *The Benthic Boundary Layer: Transport Processes and Biogeochemistry*; Boudreau, B. P.; Jørgensen, B. B., Eds.; Oxford University Press: Oxford, 2001.

(4) Kuzyakov, Y.; Blagodatskaya, E. Microbial Hotspots and Hot Moments in Soil: Concept & Review. *Soil Biol. Biochem.* **2015**, *83*, 184−199.

(5) Shapiro, O. H.; Fernandez, V. I.; Garren, M.; Guasto, J. S.; Debaillon-Vesque, F. P.; Kramarsky-Winter, E.; Vardi, A.; Stocker, R. Vortical Ciliary Flows Actively Enhance Mass Transport in Reef Corals. *Proc. Natl. Acad. Sci. U.S.A.* **2014**, *111* (37), 13391−13396.

(6) Santegoeds, C. M.; Schramm, A.; Beer, D. D. Microsensors as a Tool to Determine Chemical Microgradients and Bacterial Activity in Wastewater Biofilms and Flocs. *Biodegradation* **1998**, *9* (3/4), 159−167.

(7) Fenchel, T.; Finlay, B. Oxygen and the Spatial Structure of Microbial Communities. *Biol. Rev.* **2008**, *83* (4), 553−569.

(8) Revsbech, N. P. Analysis of Microbial Communities with Electrochemical Microsensors and Microscale Biosensors. In *Methods in Enzymology*; Elsevier, 2005; Vol. *397*, pp 147−166.

(9) Revsbech, N. P. Simple Sensors That Work in Diverse Natural Environments: The Micro-Clark Sensor and Biosensor Family. *Sens. Actuators, B* **2021**, *329*, No. 129168.

(10) Koren, K.; Zieger, S. E. Optode Based Chemical Imaging—Possibilities, Challenges, and New Avenues in Multidimensional Optical Sensing. *ACS Sens.* **2021**, *6* (5), 1671−1680.

(11) Schäferling, M. The Art of Fluorescence Imaging with Chemical Sensors. *Angew. Chem., Int. Ed.* **2012**, *51* (15), 3532−3554.

(12) Brodersen, K. E.; Koren, K.; Moßhammer, M.; Ralph, P. J.; Kühl, M.; Santner, J. Seagrass-Mediated Phosphorus and Iron Solubilization in Tropical Sediments. *Environ. Sci. Technol.* **2017**, *51* (24), 14155−14163.

(13) Frederiksen, M. S.; Glud, R. N. Oxygen Dynamics in the Rhizosphere of Zostera Marina: A Two-Dimensional Planar Optode Study. *Limnol. Oceanogr.* **2006**, *51* (2), 1072−1083.

(14) Koren, K.; Jakobsen, S. L.; Kühl, M. In-Vivo Imaging of O2 Dynamics on Coral Surfaces Spray-Painted with Sensor Nanoparticles. *Sens. Actuators, B* **2016**, *237*, 1095−1101.

(15) Kühl, M.; Behrendt, L.; Trampe, E.; Qvortrup, K.; Schreiber, U.; Borisov, S. M.; Klimant, I.; Larkum, A. W. D. Microenvironmental Ecology of the Chlorophyll B-Containing Symbiotic Cyanobacterium Prochloron in the Didemnid Ascidian Lissoclinum Patella. *Front. Microbiol.* **2012**, *3*, No. 402.

(16) Stich, M. I. J.; Nagl, S.; Wolfbeis, O. S.; Henne, U.; Schaeferling, M. A Dual Luminescent Sensor Material for Simultaneous Imaging of Pressure and Temperature on Surfaces. *Adv. Funct. Mater.* **2008**, *18* (9), 1399−1406.

(17) Wang, X.-d.; Wolfbeis, O. S.; Meier, R. J. Luminescent Probes and Sensors for Temperature. *Chem. Soc. Rev.* **2013**, *42* (19), 7834−7869.
(18) Brodersen, K. E.; Lichtenberg, M.; Ralph, P. J.; Kühl, M.; Wangpraseurt, D. Radiative Energy Budget Reveals High Photosynthetic Efficiency in Symbiont-Bearing Corals. *J. R. Soc. Interface* **2014**, *11* (93), No. 20130997.
(19) Klimant, I.; Kühl, M.; Glud, R. N.; Holst, G. Optical Measurement of Oxygen and Temperature in Microscale: Strategies and Biological Applications. *Sens. Actuators, B* **1997**, *38* (1−3), 29−37.
(20) Borisov, S. M.; Wolfbeis, O. S. Temperature-Sensitive Europium(III) Probes and Their Use for Simultaneous Luminescent Sensing of Temperature and Oxygen. *Anal. Chem.* **2006**, *78* (14), 5094−5101.
(21) Koren, K.; Kühl, M. A Simple Laminated Paper-Based Sensor for Temperature Sensing and Imaging. *Sens. Actuators, B* **2015**, *210*, 124−128.
(22) Kalinichev, A. V.; Zieger, S. E.; Koren, K. Optical Sensors (Optodes) for Multiparameter Chemical Imaging: Classification, Challenges, and Prospects. *Analyst* **2023**, *149* (1), 29−45.
(23) Borisov, S. M.; Vasylevska, A. S.; Krause, C.; Wolfbeis, O. S. Composite Luminescent Material for Dual Sensing of Oxygen and Temperature. *Adv. Funct. Mater.* **2006**, *16* (12), 1536−1542.
(24) Fischer, L. H.; Borisov, S. M.; Schaeferling, M.; Klimant, I.; Wolfbeis, O. S. Dual Sensing of pO2 and Temperature Using a Water-Based and Sprayable Fluorescent Paint. *Analyst* **2010**, *135* (6), 1224−1229.
(25) Zieger, S. E.; Steinegger, A.; Klimant, I.; Borisov, S. M. TADF-Emitting Zn(II)-Benzoporphyrin: An Indicator for Simultaneous Sensing of Oxygen and Temperature. *ACS Sens.* **2020**, *5* (4), 1020−1027.
(26) Zach, P. W.; Freunberger, S. A.; Klimant, I.; Borisov, S. M. Electron-Deficient Near-Infrared Pt(II) and Pd(II) Benzoporphyrins with Dual Phosphorescence and Unusually Efficient Thermally Activated Delayed Fluorescence: First Demonstration of Simultaneous Oxygen and Temperature Sensing with a Single Emitter. *ACS Appl. Mater. Interfaces* **2017**, *9* (43), 38008−38023.
(27) Otto, S.; Dorn, M.; Förster, C.; Bauer, M.; Seitz, M.; Heinze, K. Understanding and Exploiting Long-Lived near-Infrared Emission of a Molecular Ruby. *Coord. Chem. Rev.* **2018**, *359*, 102−111.
(28) Cai, T.; Jung, J.; Li, D.; Kim, M.; Jeon, C.-H.; Kim, K. C. Simultaneous Sensing of Oxygen Concentration and Temperature Utilizing Rise and Decay of the Phosphorescence of Y2O3:Eu3+ in High-Temperature Environments. *Sens. Actuators, B* **2022**, *370*, No. 132394.
(29) Schwendt, G.; Borisov, S. M. Achieving Simultaneous Sensing of Oxygen and Temperature with Metalloporphyrins Featuring Efficient Thermally Activated Delayed Fluorescence and Phosphorescence. *Sens. Actuators, B* **2023**, *393*, No. 134236.
(30) Larsen, M.; Borisov, S. M.; Grunwald, B.; Klimant, I.; Glud, R. N. A Simple and Inexpensive High Resolution Color Ratiometric Planar Optode Imaging Approach: Application to Oxygen and pH Sensing. *Limnol. Oceanogr. Methods* **2011**, *9* (9), 348−360.
(31) Zieger, S. E.; Mosshammer, M.; Kühl, M.; Koren, K. Hyperspectral Luminescence Imaging in Combination with Signal Deconvolution Enables Reliable Multi-Indicator-Based Chemical Sensing. *ACS Sens.* **2021**, *6* (1), 183−191.
(32) Zieger, S. E.; Koren, K. Machine Learning for Optical Chemical Multi-Analyte Imaging: Why We Should Dare and Why It's Not without Risks. *Anal. Bioanal. Chem.* **2023**, *415* (14), 2749−2761.
(33) Banala, S.; Wurst, K.; Kräutler, B. Symmetrical Tetra-B″-Sulfoleno- *Meso* -Aryl-Porphyrins — Synthesis, Spectroscopy and Structural Characterization. *J. Porphyrins Phthalocyanines* **2014**, *18*, 115−122.
(34) Wolfbeis, O. S. Editorial: Probes, Sensors, and Labels: Why Is Real Progress Slow? *Angew. Chem., Int. Ed.* **2013**, *52* (38), 9864−9865.
(35) Parker, C. A.; Hatchard, C. G. Triplet-Singlet Emission in Fluid Solutions. Phosphorescence of Eosin. *Trans. Faraday Soc.* **1961**, *57*, 1894−1904.
(36) Carraway, E. R.; Demas, J. N.; DeGraff, B. A.; Bacon, J. R. Photophysics and Photochemistry of Oxygen Sensors Based on Luminescent Transition-Metal Complexes. *Anal. Chem.* **1991**, *63* (4), 337−342.
(37) Pichette, J.; Goossens, T.; Vunckx, K.; Lambrechts, A. In *Hyperspectral Calibration Method For CMOS-Based Hyperspectral Sensors*, Proceedings Volume 10110, Photonic Instrumentation Engineering IV; Soskind, Y. G.; Olson, C., Eds.; SPIE, 2017.
(38) Bognár, Z.; Mosshammer, M.; Brodersen, K. E.; Bollati, E.; Gyurcsányi, R. E.; Kühl, M. Multiparameter Sensing of Oxygen and pH at Biological Interfaces via Hyperspectral Imaging of Luminescent Sensor Nanoparticles. *ACS Sens.* **2024**, *9* (4), 1763−1774.
(39) Lebourgeois, V.; Bégué, A.; Labbé, S.; Mallavan, B.; Prévot, L.; Roux, B. Can Commercial Digital Cameras Be Used as Multispectral Sensors? A Crop Monitoring Test. *Sensors* **2008**, *8* (11), 7300−7322.
(40) Rinnan, Å.; Andersson, M.; Ridder, C.; Engelsen, S. B. Recursive Weighted Partial Least Squares (rPLS): An Efficient Variable Selection Method Using PLS. *J. Chemom.* **2014**, *28* (5), 439−447.
(41) Bárcenas-Moreno, G.; Gómez-Brandón, M.; Rousk, J.; Bååth, E. Adaptation of Soil Microbial Communities to Temperature: Comparison of Fungi and Bacteria in a Laboratory Experiment. *Global Change Biol.* **2009**, *15* (12), 2950−2957.
(42) Nottingham, A. T.; Bååth, E.; Reischke, S.; Salinas, N.; Meir, P. Adaptation of Soil Microbial Growth to Temperature: Using a Tropical Elevation Gradient to Predict Future Changes. *Global Change Biol.* **2019**, *25* (3), 827−838.

https://doi.org/10.1021/acsmeasuresciau.4c00040
ACS Meas. Sci. Au 2024, 4, 568−576